Achieving high overall energy storage performance of KNN-based transparent ceramics by ingenious multiscale designing

Zixiong Sun[a,b,c,d,e], Shibo Zhao[a], Ting Wang[c], Hongmei Jing[f*], Qing Guo[a], Ruyue Gao[a], Liming Diwu[a], Kang Du[g] Yongming Hu[b*], Yongping Pu[e*]*

a School of Electronic Information and Artificial Intelligence, Shaanxi University of Science and Technology, Xi'an 710021, PR China

b Hubei Key Laboratory of Micro-Nanoelectronic Materials and Devices, Hubei University, Wuhan 430062, China

c Guangdong Provincial Key Laboratory of Electronic Functional Materials and Devices, Huizhou University, Huizhou 516001, Guangdong, China.

d School of Materials Science and Engineering, Shaanxi University of Science and Technology, Xi'an 710021, PR China

e MESA$^+$ Institute for Nanotechnology, University of Twente PO Box 217, 7522 NH Enschede, The Netherlands

f School of Physics and Information Technology, Shaanxi Normal University, Xi'an, 710119, PR China

g School of Mathematical and Physical Sciences, Wuhan Textile University, Wuhan, 430200, China

**Corresponding author: Zixiong Sun, Hongmei Jing, Yongming Hu, Yongping Pu*

E-mail address: SunZX@sust.edu.cn, jhmei.dengdai@snnu.edu.cn, huym@hubu.edu.cn, puyongping@sust.edu.cn

Supplementary Information

1. Calculation of W_{rec} and η

The energy storage density(*ESD*) and η of a dielectric capacitor under a specific applied electrical field (*E*) can be represented by the following formula:

$$W_{\text{rec}} = \int_{P_{max}}^{P_r} E\mathrm{d}P \qquad \text{Eq. S1}$$

$$W_{\text{char}} = \int_{0}^{P_{max}} E\mathrm{d}P \qquad \text{Eq. S2}$$

$$\eta = W_{rec}/W_{sto}100\% \qquad \text{Eq. S3}$$

in which the W_{rec} and $W_{char,}$ are the *ESD* and energy-charged density(*ECD*) during one charge-discharge process, respectively. *P* is the generated polarization under *E*, and the P_m and P_r are the maximum polarization upon charging and the remanent polarization when the electrical field returns to zero, respectively.

2. Experimental procedure

1.1. Fabrication of (1-x)$K_{0.5}Na_{0.5}NbO_3$-x$(Ba_{0.9}Ca_{0.1})(Zr_{0.15}Ti_{0.85})O_3$ ceramics

(1-*x*)$K_{0.5}Na_{0.5}NbO_3$-*x*$(Ba_{0.9}Ca_{0.1})(Zr_{0.15}Ti_{0.85})O_3$ ceramics (x=0, 0.10, 0.15, 0.20, 0.3, 0.5, 1) were manufactured via a conventional solid-state reaction method. High-purity Nb_2O_5(99.5%), Na_2O_3(99%), K_2CO_3(99.8%), $BaCO_3$ (99%), $CaCO_3$(99%), TiO_2 (99.9%), ZrO_2 (99.8%) powders were used as the raw materials. The raw materials were accurately weighed according to the stoichiometric ratio of each ceramics component and ball-milled in a planetary ball mill with zirconia balls and anhydrous ethanol as the medium for 12 h. The resulting slurry was dried in an oven at 80 ^oC and then placed into an alumina crucible to be pre-burned at 900 ^oC for 4 h. After pre-burning, the powder underwent a second ball milling for 12 h, followed by drying and the addition of a 5 *wt*% (mass fraction) polyvinyl alcohol (PVA) solution as a binder. Pellets were then formed under a pressure of 16 MPa to create discs with a diameter of 10 mm and a thickness of approximately 2 mm. The pellets were sintered at 1160-1400℃ for 4h with a heating rate of 3℃ min^{-1} to obtain ceramic samples.

1.2. Characterization

The crystal structure of (1-x)$K_{0.5}Na_{0.5}NbO_3$-*x*$(Ba_{0.9}Ca_{0.1})(Zr_{0.15}Ti_{0.85})O_3$ ceramics was measured via X-ray diffraction (XRD, *D8 Advance, Bruker*). The microstructures of the sintered ceramic samples were observed using scanning electron microscopy (SEM, *Zeiss Sigma 300*). The average grain size of the as-prepared specimens was counted by Nano Measurer Software with a statistical grain number of >100. The high-angle transmission electron microscope annular dark field measurements were performed by transmission electron microscopy (*FEI Titan Cubed Themis G2 300*). The dielectric properties were measured using

an impedance analyzer *(E4980A, Agilent Technologies*) in the frequency range from 1 kHz to 1 MHz and the temperature range from 25 °C to 500 °C. To test the ferroelectric properties and pulse discharge behavior, the sintered ceramics were polished to a thickness of 120-100 μm, and then gold electrodes with a radius of 2 mm were sputtered on the surface. The corresponding *P-E* loops were obtained via a ferroelectric integrated test system (*Premier II, Radiant*), and the discharge curves of 0.7KNN-0.3BCZT ceramic were recorded using a charging-discharging measurement system (*CFD-003, Tongguo technology*). The forbidden bandwidths were acquired by the ultraviolet and visible (UV-vis) absorption spectra (*Cary 5000*). The chemical states of the KNN-BCZT system were recorded by X-ray photoemission spectroscopy (XPS, *PHI 5000 Versaprobe III, ULVAC-PHI*). The band-gap energy of the ceramics was measured by ultraviolet-visible (UV-Vis) spectrophotometer (*UV-3600; Shimadzu, Tokyo, Japan*). The transmittance of the samples was evaluated in the wavelength range of 100 nm to 850 nm using a spectrophotometer (UV-2550; Shimadzu Co, Tokyo, Japan).

1.3. The FORC distribution.

The FORC method is based on the Preisach model and assumes the hysteresis loop consists of many minor loops (named "hysterons"). In the *FORC* measurement, the electric field decreases from the positive saturation field E_{max} to E_r with an interval ΔE. We can calculate the "hysterons" distribution through a set of *FORC* loops by following formulas[1,2]:

$$\rho(E_r,E) = \frac{1}{2}\frac{\partial P^2(E_r,E)}{\partial E_r \partial E} \qquad \text{Eq. S4}$$

where $\rho(E_r,E)$ is the distribution density, E_r is the reversal electric field, and E is the real electric field. In this work, we set E_{max} as 180 MV/cm and ΔE as 20 MV/cm and measured 60 FORC loops for calculation. (Fig S3) We calculate the "hysterons" distribution and plot the contour

plot as a function of E and E_r.

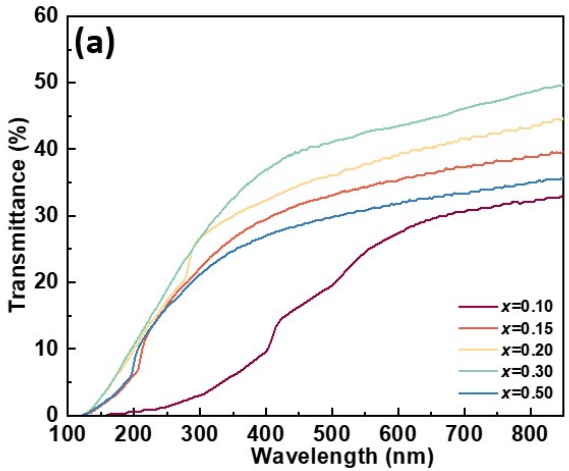

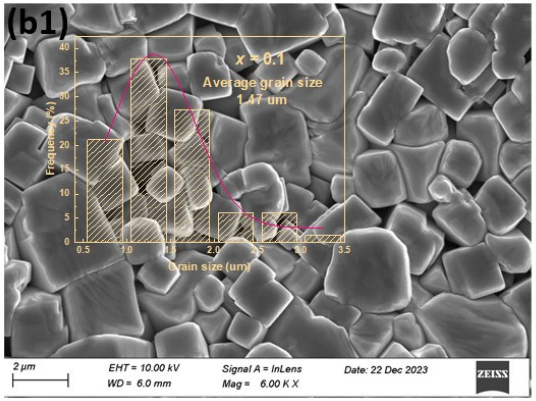

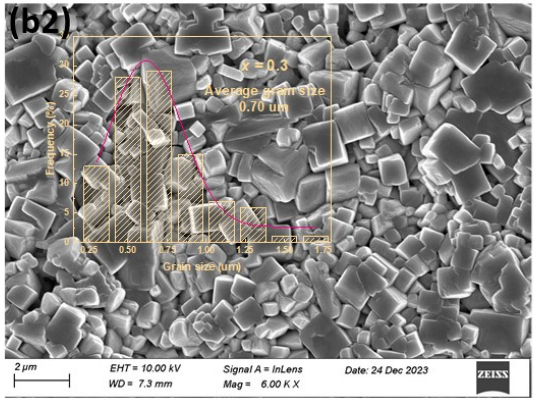

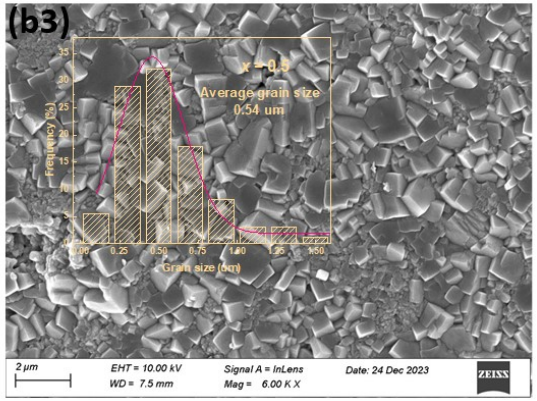

Figure S1 (a) optical transmittance diagrams of (1-*x*)KNN-*x*BCZT ceramics; (b1)-(b3) the SEM image of (1-*x*)KNN-*x*BCZT ceramics with *x*=0.1, 0.3, and 0.5, which are the grain size distribution inserted in each figure.

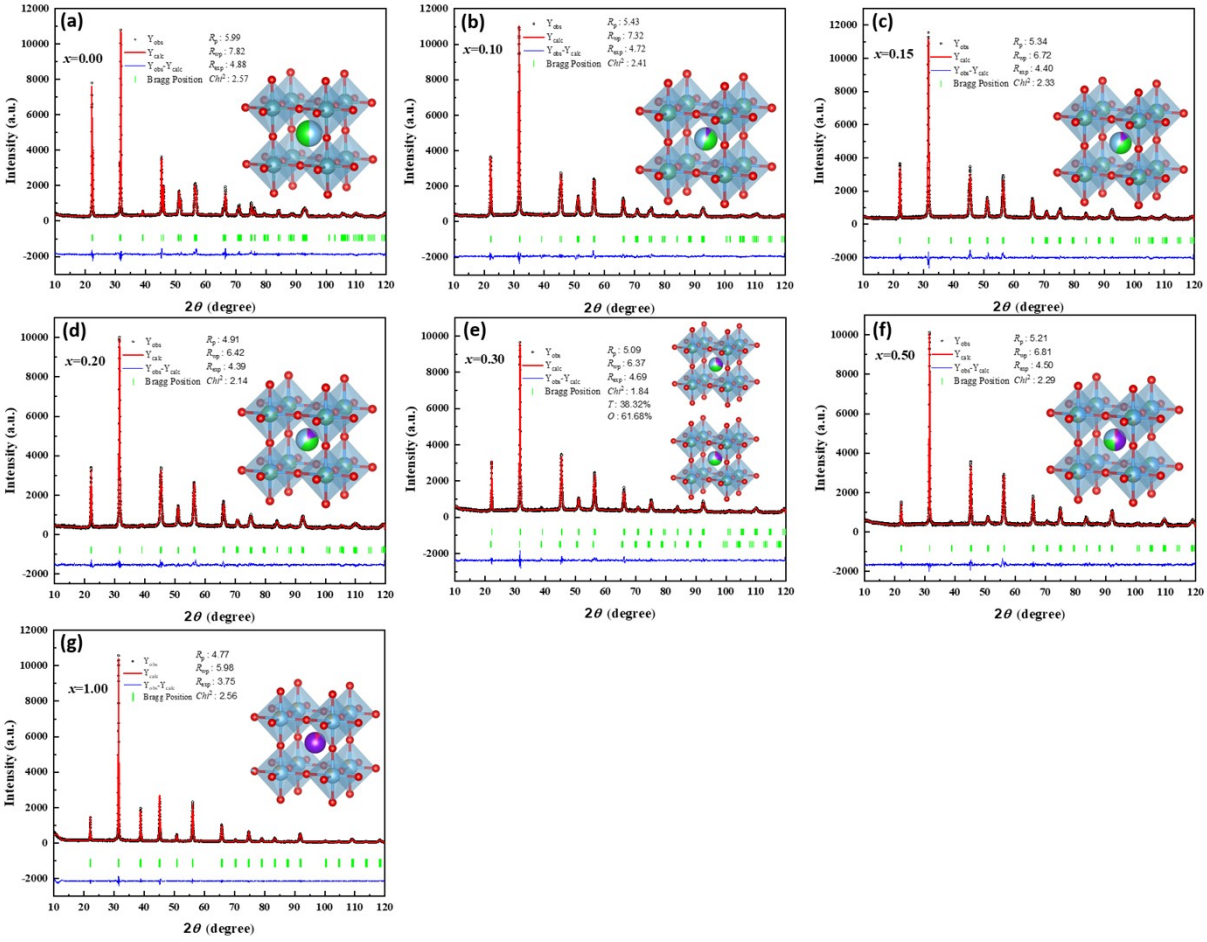

Figure S2 the Rietveld XRD refinement of all the (1-*x*)KNN-*x*BCZT ceramics, and the lattice parameters with ball-stick models are inserted in each figure.

Tab. S1 Parameters of the Rietveld XRD refinement result and the phase content of (1-*x*)KNN-*x*BCZT.

	x=0.00	*x*=0.10	*x*=0.15	*x*=0.20	*x*=0.30(*T*)	*x*=0.30(*O*)	*x*=0.50	*x*=1.00
a	5.638	3.976	3.982	3.986	3.992	4.005	4.007	4.014
b	3.943	3.976	3.982	3.986	3.992	4.005	4.007	4.014
c	5.672	4.011	4.009	4.007	4.005	4.002	3.999	3.995
$\boldsymbol{chi^2}$	2.57	2.41	2.33	2.14	1.84		2.29	1.40
$\boldsymbol{R_p}$	5.99	5.43	5.34	4.91	5.09		5.21	6.57
$\boldsymbol{R_{wp}}$	7.82	7.32	6.72	6.42	6.37		6.81	8.78
$\boldsymbol{R_{exp}}$	4.88	4.72	4.40	4.39	4.69		4.50	7.42

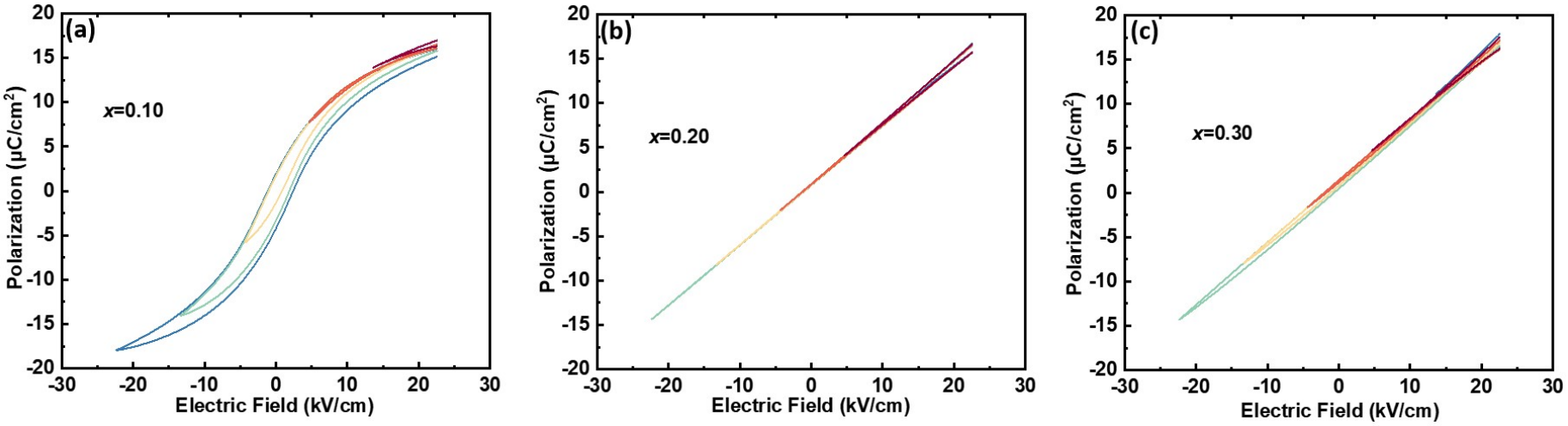

Figure S3 (a)-(c) the FORC loop of the (1-*x*)KNN-*x*BCZT with *x*=0.10, 0.20, and 0.30.

3. *Wei-bull* distribution

Before calculating the energy storage density(W_{rec}), the electric breakdown strength(E_b) of each film should be confirmed by employing the *Weibull* distribution, which can be expressed as follows:

$$X_i = \ln E_i \quad \text{Eq. S5}$$

$$Y_i = \ln(-\ln(1 - P_i)) \quad \text{Eq. S6}$$

$$P_i = \frac{i}{1 + n} \quad \text{Eq. S7}$$

Where X_i and Y_i are the two parameters of the Weibull distribution, Y_i varies linearly with X_i with a slope of β, E_i, and P_i are the sample's breakdown field and the electric field's failure probability distribution, respectively. While n, i, and β are the total number of specimens, the serial number of dielectric strength, and the slope of the linear relationship between $\ln(E_i)$ and $\ln(-\ln(1-P_i))$, respectively.

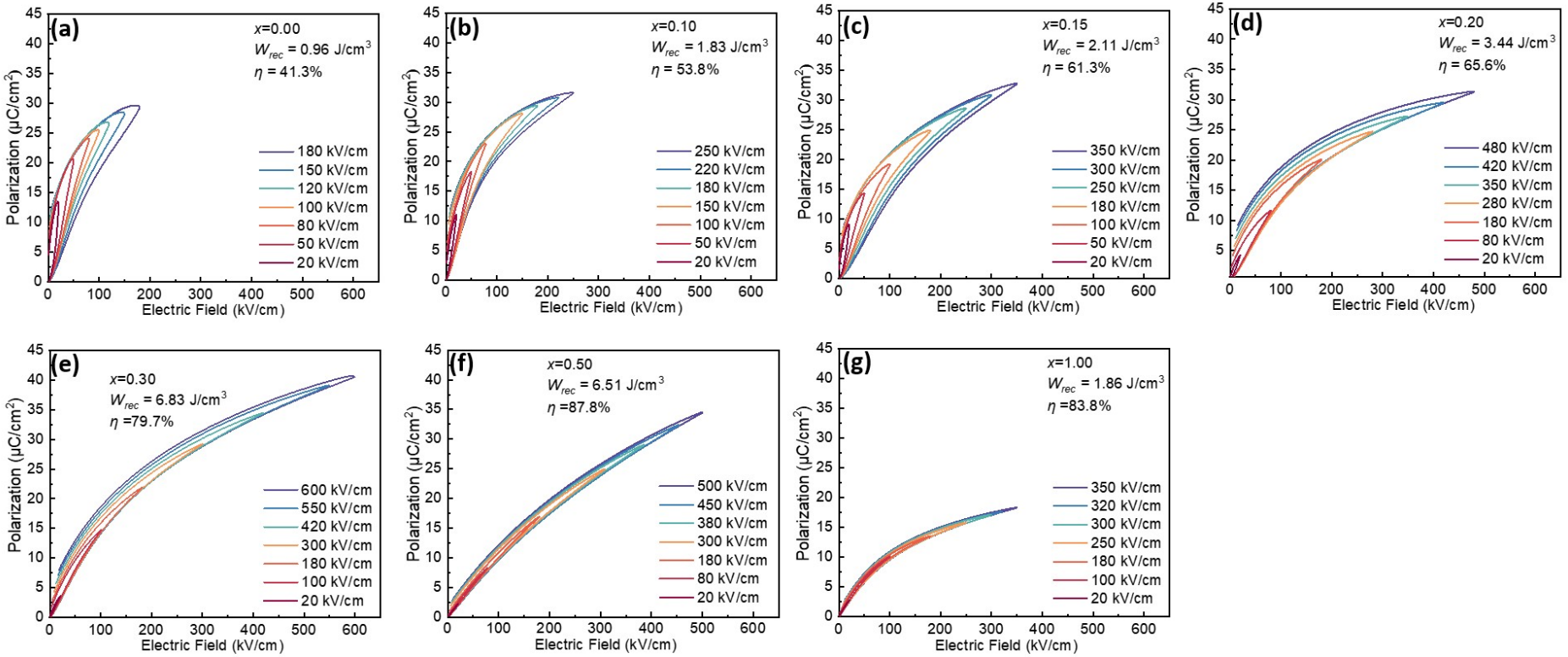

Figure S4 (a)-(h) unipolar P-E loops of the (1-*x*)KNN-*x*BCZT with *x*=0.00-1.00 at different electric fields.

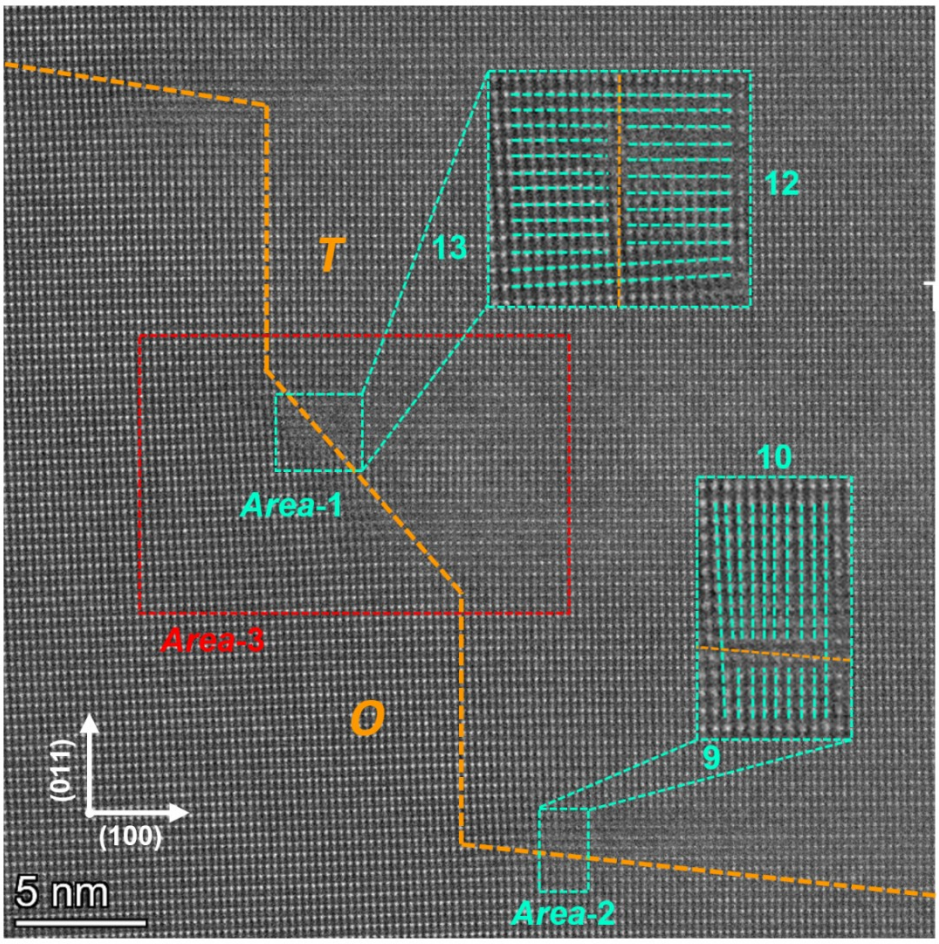

Figure S5 the HAADF-STEM images of (1-*x*)KNN-*x*BCZT with *x*=0.3 along [110] crystal axis

4. Discussion of the contribution of the interfacial polarization

In general, dielectric materials, which are made up of atoms or molecules, possess four basic types of electric polarization: electronic polarization, ionic polarization, dipole/orientational polarization, and interfacial/space charge polarization. Each of them requires different times to switch, which results in a decrease in dielectric constants with increasing electric field frequency. The total polarization of one dielectric material can be written as:

$$P = (\varepsilon_r - 1)\varepsilon_0 E = N\alpha E \quad \text{Eq. S8}$$

in which E is the applied external electric field on the dielectric material, and P is the total polarization triggered by E. The ε_r and ε_0 are the material's dielectric constants (or relative permittivity) and the vacuum permittivity, which equals $8.854*10^{-12}$ F/m, respectively. N is the number of induced dipole moments in unit volume, and the α is the polarizability of the dielectric.

When under static *DC* fields (applied electric frequency f=0), the contribution to P in Eq. S8 involves all the types of electric polarization mentioned above. The polarization contributed by the electronic polarization, ionic polarization, and orientational polarization can be written as:

$$P' = (\varepsilon_{r\infty} + \varepsilon_{ro} - 1)\varepsilon_0 E = N(\alpha_\infty + \alpha_o)E \quad \text{Eq. S9}$$

in which the $\varepsilon_{r\infty}$ and ε_{ro} are the dielectric constant when $f \rightarrow \infty$ and the dielectric constant contributed by the orientational polarization, respectively. Thus, the interfacial polarization (Pi) of a dielectric material should be:

$$P_i = P - P' = (\varepsilon_r - \varepsilon_{r\infty} - \varepsilon_{ro} - 1)\varepsilon_0 E = N(\alpha - \alpha_\infty - \alpha_o)E \quad \text{Eq. S10}$$

and the corresponding polarizability for the interfacial polarization should be :

$$\alpha_i = \alpha - \alpha_\infty - \alpha_o = (\varepsilon_r - \varepsilon_{r\infty} - \varepsilon_{ro})\varepsilon_0/N \qquad \text{Eq. S11}$$

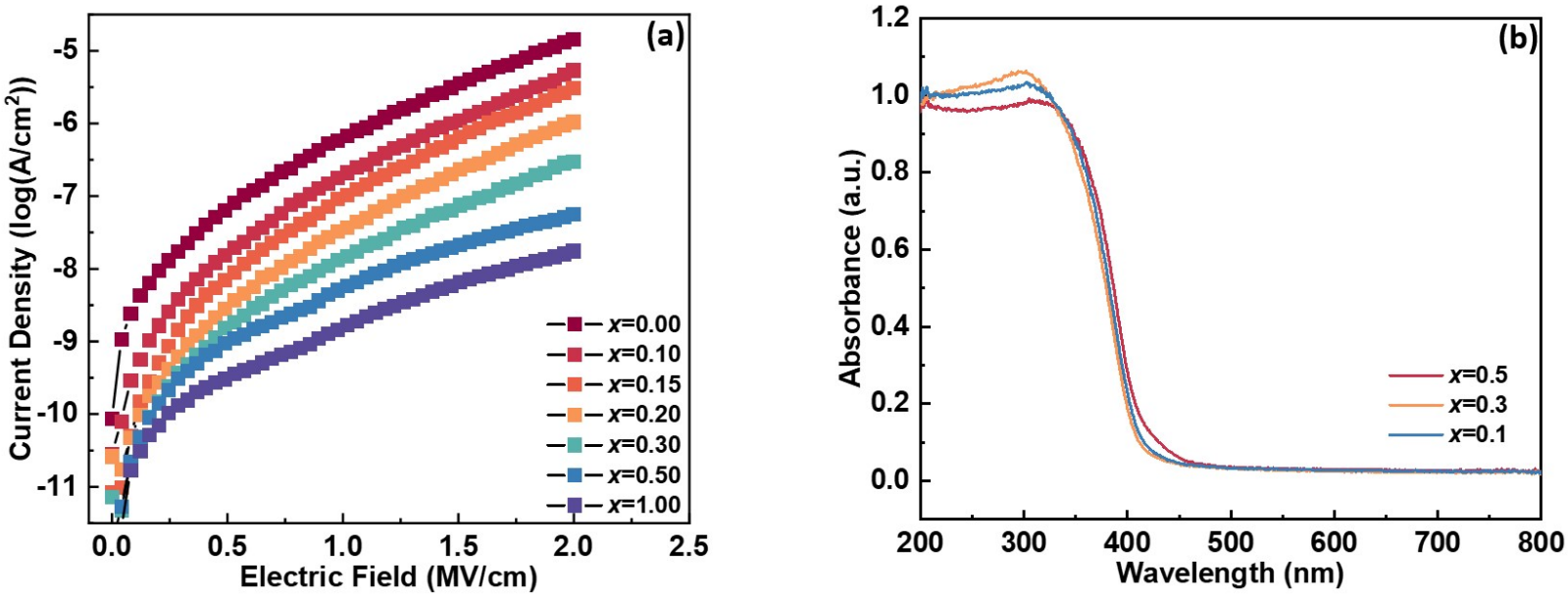

Figure S6 (a) the relationship between the current density and the electric field(*J-E* curves) of all the ceramics; (b) the UV-vis absorption spectra of (1-*x*)KNN-*x*BCZT ceramic with *x*=0.1, 0.3, and 0.5

5. Formation of the band diagram

4.1 formation of the Schottky emission mode

Fig. S7(a1) shows the ideal band diagram of both the Pt electrode and the (1-*x*)KNN-*x*BCZT ceramic with a smaller *x* before contact. As the work function of the Pt electrode(Φ_E) is higher than that of (1-*x*)KNN-*x*BCZT ceramics[3-5], once connected, the Fermi level of both electrode($E_{F\text{-}E}$) and ceramic($E_{F\text{-}C}$) should be aligned, which leads to band bending in the interface. According to the defect reaction Eq. 1-9, the majority carriers of (1-*x*)KNN-*x*BCZT ceramics should be electrons, and thus, the ceramic can be regarded as *n*-type semiconductors[6]. When contacted, the electrons would drift from the ceramic side to the electrode side, and a depletion layer(R_d) with the direction pointing to Au formed in the interface formed, as displayed in Fig. S7 (a2). More electrons will be trapped in $R_{d,}$ and finally, a build-in potential(Φ_b) formed. When applying a forward external voltage(V) pointing from ceramic to electrode, as seen in Fig. S7 (a3), the $E_{F\text{-}C}$ moves down, increasing the Φ_b to Φ_b+V and R_d to R_d'. In this case, more electrons were trapped in the interface.

4.2 formation of the Ohmic contact mode

The deviated band diagram of the Pt electrode and the (1-*x*)KNN-*x*BCZT ceramic with a larger *x* before contact is shown in Fig. S7(b1). Due to the newly-formed $V_O^{\cdot\cdot}$, as expressed from Eq. 1 to 9, the electron affinity of the ceramics(χ_C) increases and their $E_{F\text{-}C}$ moves down and is lower than the $E_{F\text{-}E}$. When contact, as seen in Fig. S7(b2), the electrons flow from the electrode side to the ceramic side until an equilibrium is established. Then, the electrons accumulated in the Pt/(1-x)KNN-xBCZT interface further prevent such an electron's movement, and the $E_{F\text{-}E}$ and $E_{F\text{-}C}$ will be aligned, leading to the band bending. When applying a forward external

voltage(V) pointing from ceramic to electrode, as seen in Fig. S7 (b3), the V will force the electrons to flow from the electrode side to the ceramic side, leading to only a small interface barrier(Φ_i) without depletion region. In this case, almost no electron can be trapped in the Pt/(1-x)KNN-xBCZT interface.

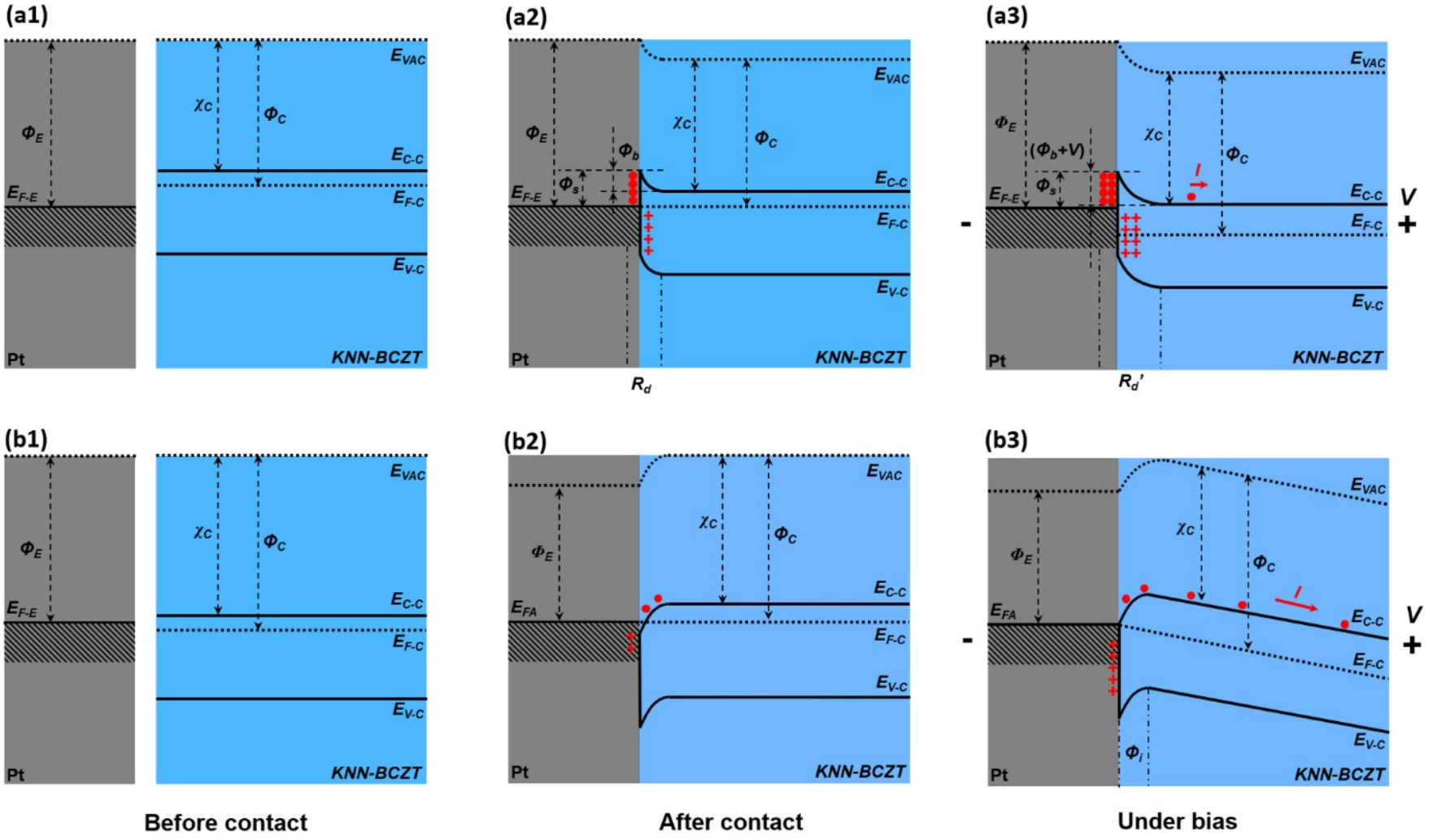

Figure S7 the band diagrams to show the formation of these two different kinds of conductive mechanisms

6. The physical meaning of the abbreviations in the band diagram analyzing

E_{VAC}: the vacuum level

$E_{F\text{-}E}$: the Fermi energy level of the Pt electrode

$E_{F\text{-}C}$: the Fermi energy level of the (1-*x*)KNN-*x*BCZT ceramics

$E_{C\text{-}C}$: the conduction band of the (1-*x*)KNN-*x*BCZT ceramics

$E_{V\text{-}C}$: the valence band of the (1-*x*)KNN-*x*BCZT ceramics

Φ_E: the work function of the Pt electrode

Φ_C: the work function of the (1-*x*)KNN-*x*BCZT ceramics

χ_C: the electron affinity of the (1-*x*)KNN-*x*BCZT ceramics

ϕ_s: the Schottky barrier height

ϕ_b: the build-in potential

V: the externally applied voltage

R_d: the depletion region without V

R_d': the depletion region under V

ϕ_i: the interface barrier

7. Finite Element Simulation

The *COMSOLMultiphysics6.0* linking with *Matlab5.2* was employed to simulate the potential and electric field distribution and the current spread. The *Voronoi* diagram in *Matlab5.2* was chosen to describe the geometry of the BCZT-*x*BZT ceramics, and each polygon was identified as one ferroelectric domain. Compared to the *T*-phase in the BCZT-0.02BZT, the *T*-phase in the BCZT-0.15BZT was set to have a smaller domain size and quantity to fit the microstructure characterization.

Once the breakdown happens, the film will undergo an irreversible transformation, widely believed to be the joint effect of electric and thermal fields. Based on this, the *AC/DC module* and *heat transfer module* in *COMSOLMultiphysics6.0* are both called, and the physical model can be expressed as follows:

The electrical breakdown process was described according to the spread of current density with the boundary conditions meeting:

$$\boldsymbol{n}\cdot\boldsymbol{i}=0 \qquad \text{Eq. S12}$$

where $\boldsymbol{n}$ and $\boldsymbol{i}$ are the normal vector and current density vector, respectively. This boundary condition means that no electric current flows into the boundary. The constitutive relations are expressed as:

$$\boldsymbol{J}=\sigma\boldsymbol{E} \qquad \text{Eq. S13}$$

$$\boldsymbol{J}=A^{*}T^{2}\exp\left[\frac{-q(\phi_S-\sqrt{q\boldsymbol{E}/4\pi\varepsilon_r\varepsilon_0})}{kT}\right] \qquad \text{Eq. S14}$$

which is the standard Ohmic's contact and Schottky contact, respectively, and

$$\boldsymbol{D}=\varepsilon_0\varepsilon_r\boldsymbol{E} \quad \text{Eq. S15}$$

where $\boldsymbol{J}$ and $\boldsymbol{E}$ are the current density and external electrical field, respectively, and σ and ε_r are each material's electrical conductivity and dielectric constant (permittivity), which needs input in the model. ε_0 is vacuum permittivity with a value of $8.854187817*10^{-12}$ F/m. The A^*, k, q, ε_0, and ε_r, which won't change with external factors, are the effective Richardson constant, Boltzmann's constant, electronic charge, vacuum dielectric constant, and relative dielectric constant, respectively. In this work, the Ohmic's contact was applied in the BCZT-xBZT ceramics with x=0.02 and 0.22(Eq. S12), and the Schottky contact was applied in that with x=0.15(Eq. S14), and the Schottky barrier height was used as 1.4 eV. The dielectric constant of the *T*-phase, which is marked with the *T* in each domain is filled with ~10000 and the *C*-phase, which is the rest part of each ceramic, has a dielectric constant of ~7000.

Considering the stationary equation of continuity of the model after a long time, Eq. S13 and 14 should be changed to a more general form:

$$\boldsymbol{J}=\sigma\boldsymbol{E}+\frac{\partial \boldsymbol{D}}{\partial t}+\boldsymbol{J_e} \quad \text{Eq. S16}$$

$$\boldsymbol{J}=A^*T^2\exp\left[\frac{-q(\emptyset_S-\sqrt{q\boldsymbol{E}/4\pi\varepsilon_r\varepsilon_0})}{kT}\right]+\frac{\partial \boldsymbol{D}}{\partial t}+\boldsymbol{J_e} \quad \text{Eq. S17}$$

At the same time, current conservation should be met from then on with the equations:

$$\nabla\cdot\boldsymbol{J}=Q_{j.v} \quad \text{Eq. S18}$$

$$\boldsymbol{E}=-\nabla V \quad \text{Eq. S19}$$

where $Q_{j.v}$ and $\boldsymbol{D}$ represent the change rate of electric charge per unit volume and the electric

displacement vector. $\boldsymbol{J_e}$ is the current density and density of the external electric current, and V denotes the electrical potential. Here, we use the *If sentence*, which is written as *if(ht. alpha>0.1,6e6,0.04)* and was input in the software to determine if a breakdown occurred or not. It means if the breakdown happens, the σ takes the 6e6; otherwise, it takes 0.04. The *ht. alpha* is the physical name of $\frac{\partial \alpha}{\partial t}$, which represents an anisotropic thermal diffusivity(α).

The heat transfer in solid interface solves for the following equation derived from:

$$d_z(\rho C_p)_{eff}\frac{\partial T}{\partial t} + d_z(\rho C_p)_{\text{eff}}\boldsymbol{u}\cdot\nabla T + \nabla\cdot\boldsymbol{q} = d_z Q + q_0 + d_z Q_{ted} \quad \text{Eq. S20}$$

in which the $\boldsymbol{u}$ is the fluid velocity vector, and the $\boldsymbol{q}$ is the conductive heat flux that is written as:

$$\boldsymbol{q} = -d_z k_{eff}\nabla T \quad \text{Eq. S21}$$

and the d_z, $k_{eff,}$ and ∇T are the domain thickness in the out-of-plane direction, effective thermal conductivity, and temperature perturbation, respectively. The $(\rho Cp)_{eff}$ is the effective volumetric heat capacity at constant pressure that is composed of two parts:

$$(\rho C_p)_{eff} = \theta_{it}k_{it} + (1 - \theta_{it})k \quad \text{Eq. S22}$$

where the θ_{it} and k are the fraction of transformation and thermal conductivity, respectively, and the θ_{it} can be expressed as:

$$\theta it = \min(\alpha_b, 1) \quad \text{Eq. S23}$$

where the α_b is the fraction of film that was broken down to correspond to the whole film. The Q in Eq. S20 is the heat source and is defined as:

$$Q = -\rho L_{it,h}\frac{\partial \theta_{it}}{\partial t}(T > T_{it.h}) \quad \text{Eq. S24}$$

where the T_{it}, t_{it}, and L_{it} are the transformation temperature, transformation time, and the

enthalpy change when the electric breakdown happens.

The following formula should be satisfied when the *heat transfer module* is coupled with the *AC/DC module*.

$$\frac{\partial \alpha}{\partial t} = \frac{1}{t_{it,h}} (T > T_{it,h}) \qquad \text{Eq. S25}$$

Once the electric breakdown happens, the $\frac{\partial \alpha}{\partial t}$ changes, so the σ mentioned above also changes. In our work, the T_{it} and t_{it} are set to be 150 ^{o}C and 0.01ns, respectively, according to the literature.[8-10] The serial number of the *COMSOLMultiphysics6.0* and *Matlab5.2* is offered by the University of Twente.

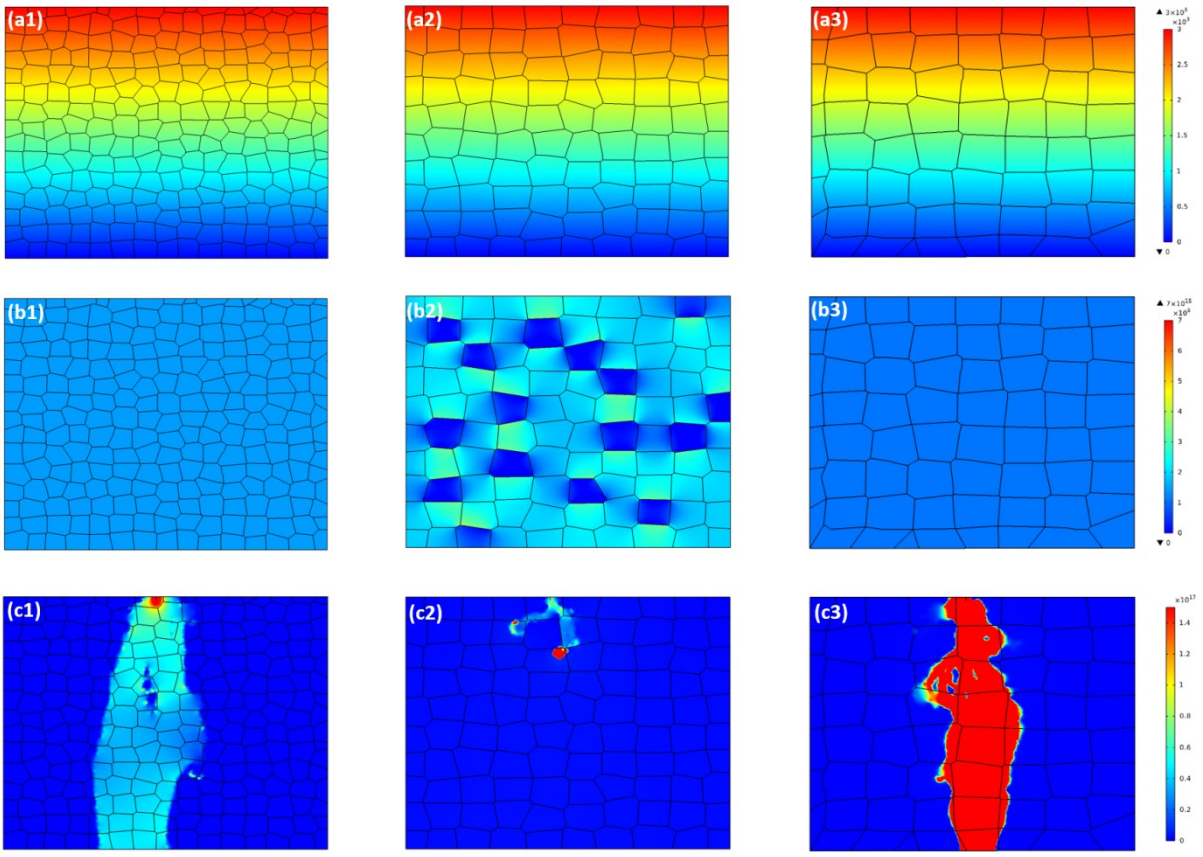

Figure S8 (a1)-(a3) the distribution of electric potential; (b1)-(b3)electric field; (c1)-(c3) current density of the (1-*x*)KNN-*x*BCZT ceramics

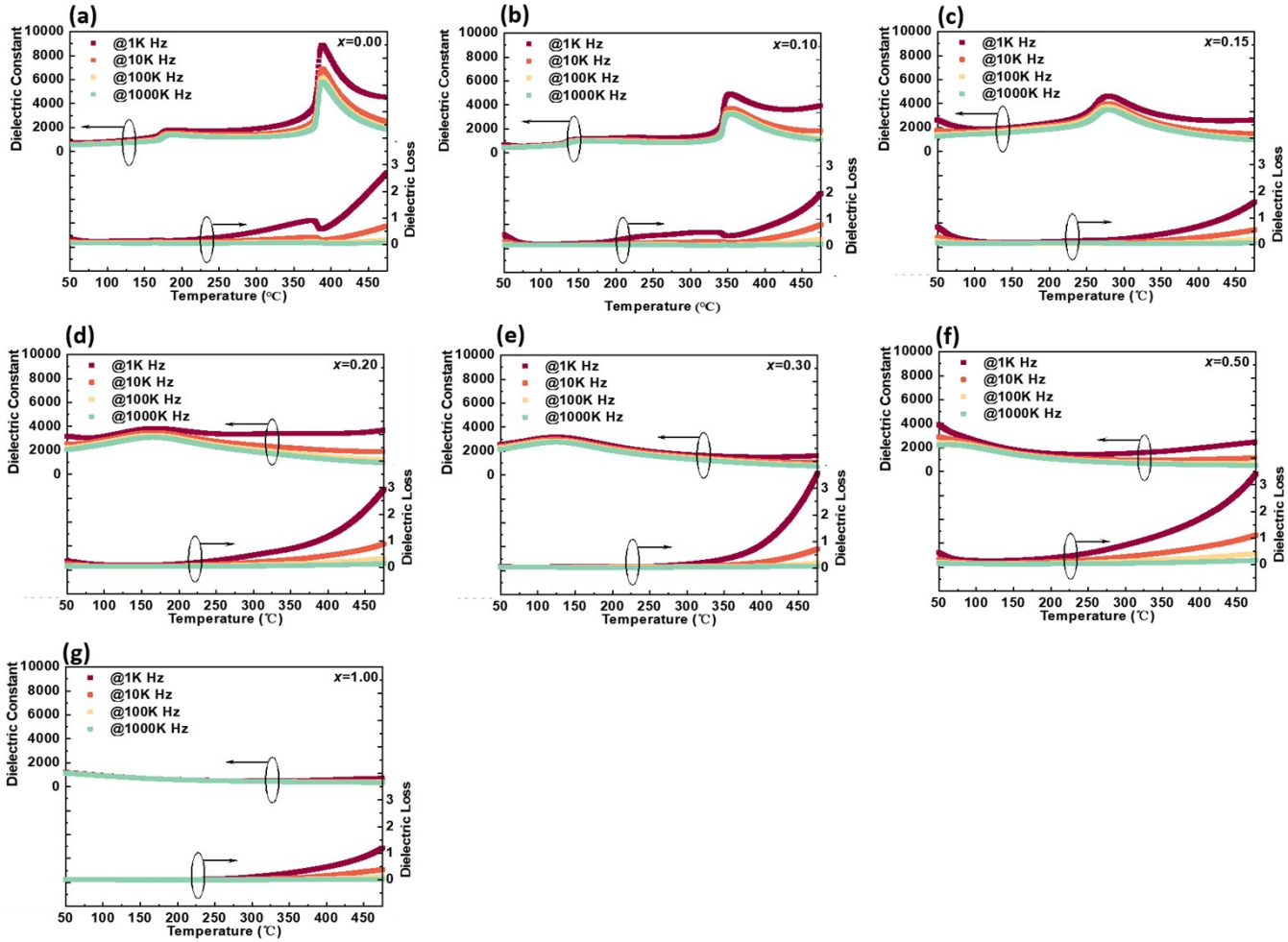

Figure S9 the temperature dependence of dielectric constant(*ε-T curve*) and dielectric loss(*tan δ-T curve*) of all the (1-*x*)KNN-*x*BCZT ceramics from 50 °C to 475 °C

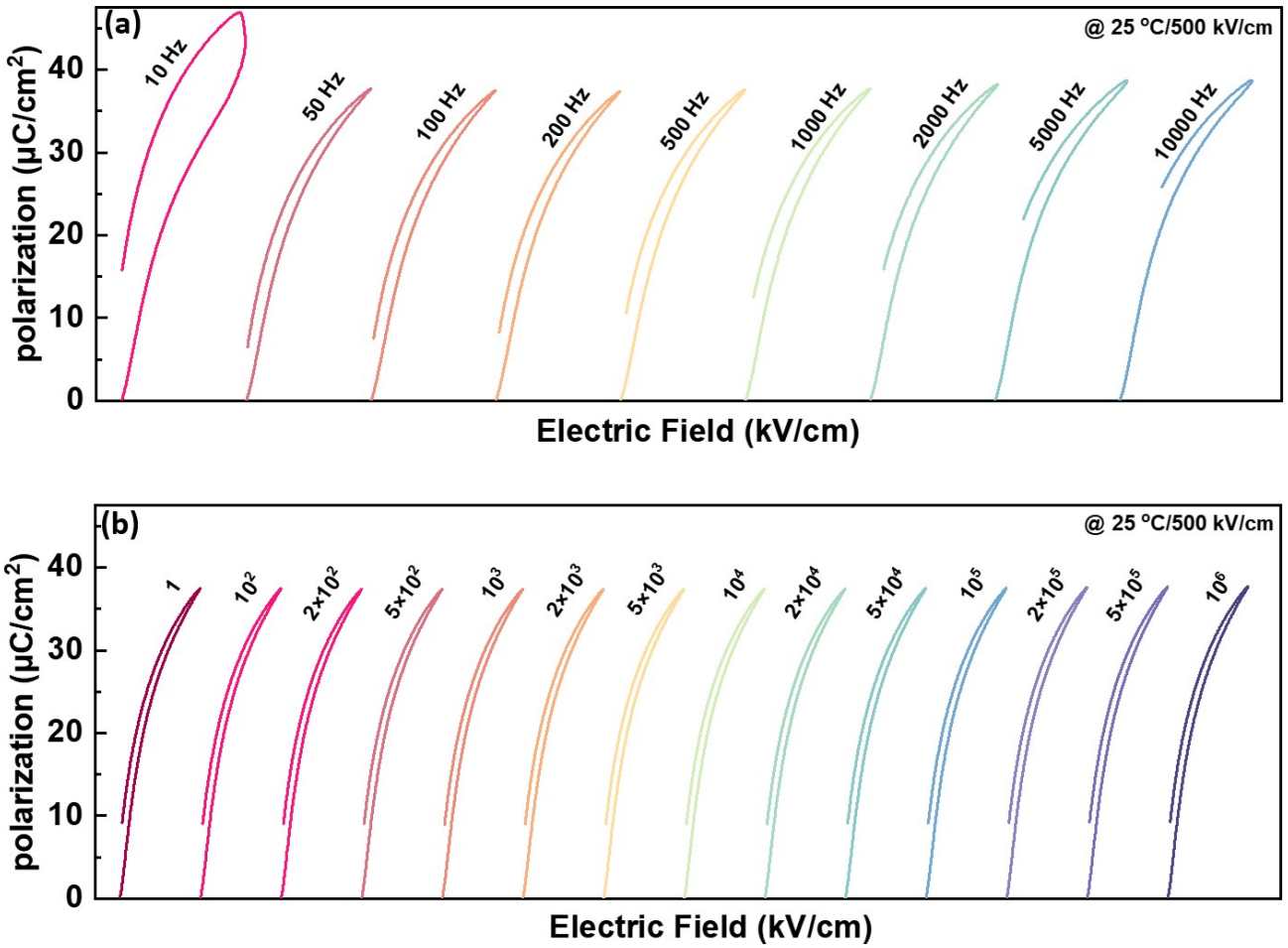

Figure S10 the unipolar *P-E* loops of the 0.7KNN-0.3BCZT measured (a) from 10^2 Hz to 10^4 Hz under 500 kV/cm at room temperature; (b) during polarization fatigue from the 1st to 10^{6th} cycle under 500 kV/cm at room temperature.

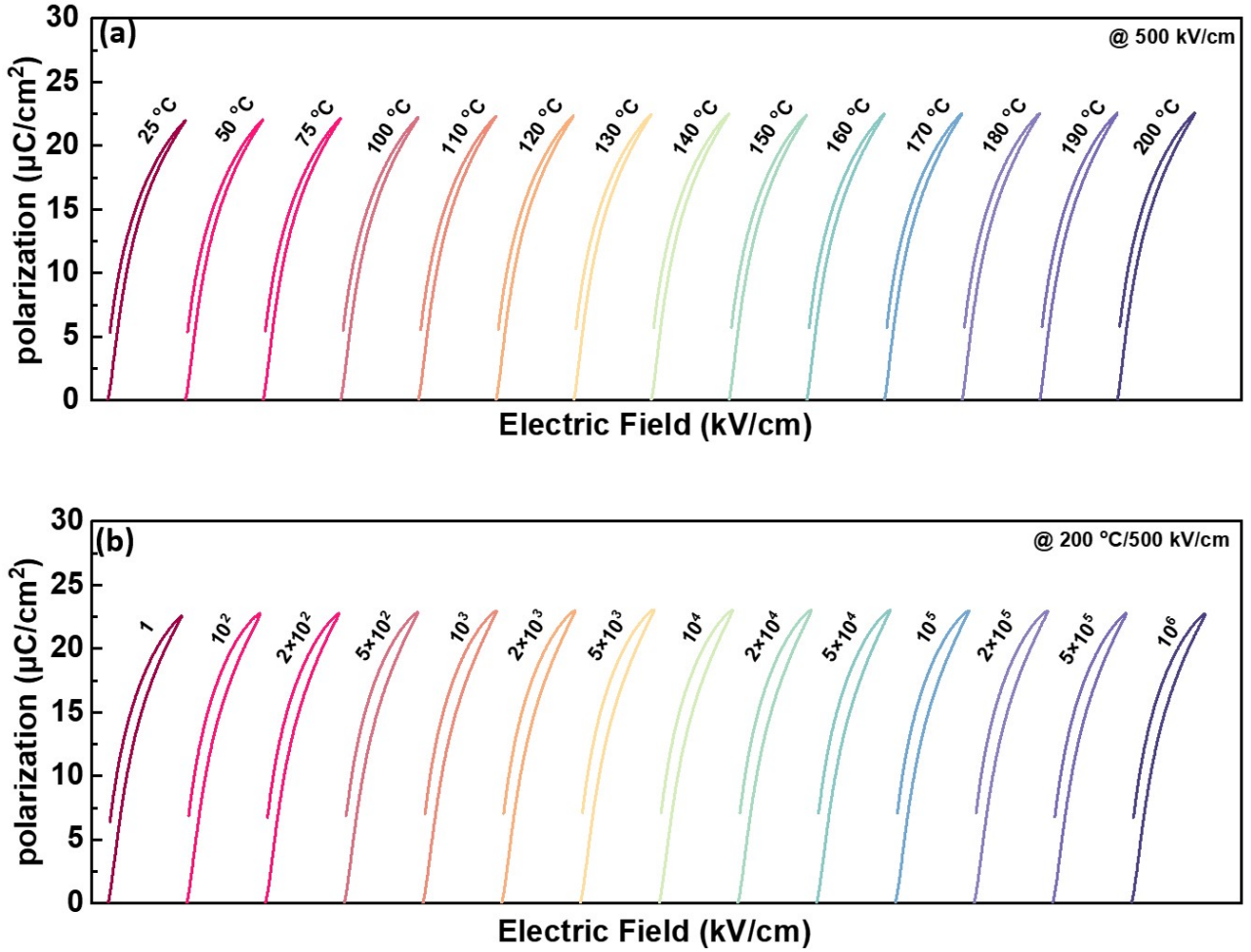

Figure S11 the unipolar *P-E* loops of the 0.7KNN-0.3BCZT measured (a) from room temperature to 200 °C at 500 kV/cm; (b) from the 1st to 10^{6th} cycle under 500 kV/cm at 200 °C.

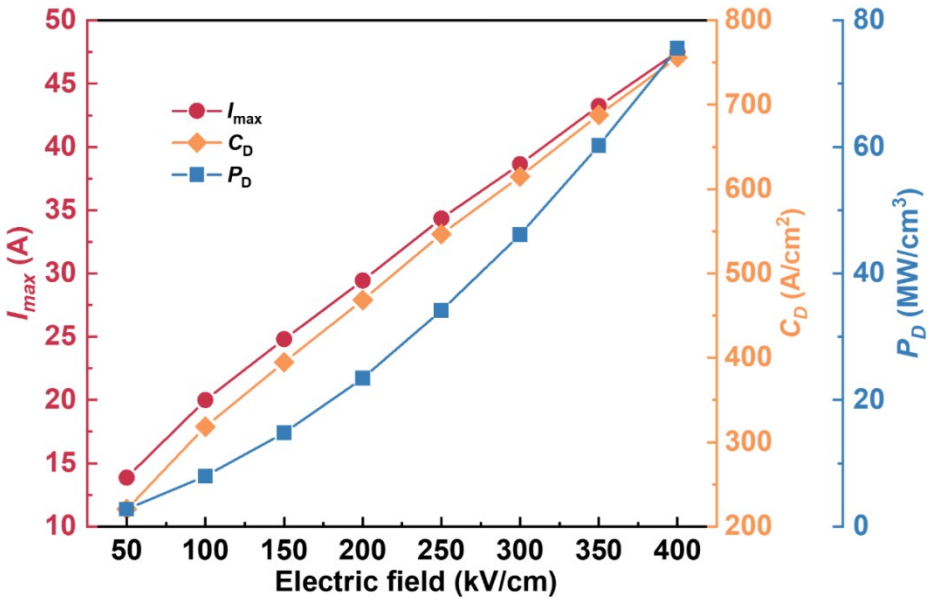

Figure S12 shows the variations between Imax, CD, PD, and applied electric fields.

References

[1] T.-Y. Hu, C. Ma, Y. Dai, Q. Fan, M. Liu and C.-L. Jia, *ACS Appl. Mater. Interfaces*, 2020, **12**, 25930–25937.

[2] C. Wang, X. Yang, Z. Wang, C. He and X. Long, *Acta Mater.*, 2019, **170**, 100–108.

[3] F. Opoku, K. K. Govender, C. G. van Sittert and P. P. Govender, *Carbon*, 2018, **136**, 187–195.

[4] Z. Sun, S. Huang, W. Zhu, Y. A. Birkhölzer, X. Gao, R. A. Avila, H. Huang, X. Lou, E. P. Houwman, M. D. Nguyen, G. Koster and G. Rijnders, *APL Mater.*, 2023, **11**,101129.

[5] Z. Sun, E. P. Houwman, S. Wang, M. D. Nguyen, G. Koster and G. Rijnders, *J. Alloys Compd.*, 2024, **981**, 173758.

[6] J. Dong, J. Han, Y. Liu, A. Nakajima, S. Matsushita, S. Wei and W. Gao, *ACS Appl. Mater. Interfaces*, 2014, **6**, 1385–1388.